

The Earliest Phases of Star formation (EPoS)

Temperature, density, and kinematic structure of the star-forming core CB 17*

M. Schmalzl^{1,2,3}, R. Launhardt², A. M. Stutz², H. Linz², T. L. Bourke³, H. Beuther², Th. Henning², O. Krause², M. Nielbock², and A. Schmiedeke^{2,4}

¹ Leiden Observatory, Leiden University, PO Box 9513, 2300 RA Leiden, The Netherlands
e-mail: schmalzl@strw.leidenuniv.nl

² Max Planck Institute for Astronomy, Königstuhl 17, 69117 Heidelberg, Germany

³ Harvard-Smithsonian Center for Astrophysics, 60 Garden Street, Cambridge, MA 02138, USA

⁴ Universität zu Köln, Zülpicher Straße 77, 50937 Köln, Germany

Received 29 June 2013 / Accepted 25 May 2014

ABSTRACT

Context. The initial conditions for the gravitational collapse of molecular cloud cores and the subsequent birth of stars are still not well constrained. The characteristic cold temperatures (~ 10 K) in such regions require observations at sub-millimetre and longer wavelengths. The *Herschel* Space Observatory and complementary ground-based observations presented in this paper have the unprecedented potential to reveal the structure and kinematics of a prototypical core region at the onset of stellar birth.

Aims. This paper aims to determine the density, temperature, and velocity structure of the star-forming Bok globule CB 17. This isolated region is known to host (at least) two sources at different evolutionary stages: a dense core, SMM1, and a Class I protostar, IRS.

Methods. We modeled the cold dust emission maps from $100\,\mu\text{m}$ to $1.2\,\text{mm}$ with both a modified blackbody technique to determine the optical depth-weighted line-of-sight temperature and column density and a ray-tracing technique to determine the core temperature and volume density structure. Furthermore, we analysed the kinematics of CB17 using the high-density gas tracer N_2H^+ .

Results. From the ray-tracing analysis, we find a temperature in the centre of SMM1 of $T_0 = 10.6$ K, a flat density profile with radius 9.5×10^3 au, and a central volume density of $n_{\text{H}_2,0} = 2.3 \times 10^5 \text{ cm}^{-3}$. The velocity structure of the N_2H^+ observations reveal global rotation with a velocity gradient of $4.3 \text{ km s}^{-1} \text{ pc}^{-1}$. Superposed on this rotation signature we find a more complex velocity field, which may be indicative of differential motions within the dense core.

Conclusions. SMM is a core in an early evolutionary stage at the verge of being bound, but the question of whether it is a starless or a protostellar core remains unanswered.

Key words. dust, extinction – ISM: molecules – ISM: kinematics and dynamics – stars: formation – stars: low-mass – ISM: individual objects: CB 17

1. Introduction

Knowledge of the initial conditions is crucial for understanding the evolution from starless to prestellar to protostellar cores (e.g., di Francesco et al. 2007). Owing to their low temperatures of $T \sim 10$ K (e.g., Bergin & Tafalla 2007; André et al. 2013), the peak of the thermal dust emission of prestellar cores is found at sub-millimetre wavelengths. Observations with millimetre and sub-millimetre bolometer arrays revealed a flattening of the radial intensity distribution in the central regions (e.g., Ward-Thompson et al. 1994, 1999; Shirley et al. 2000), which contradicted the assumption of a singular isothermal sphere (e.g., Shu 1977) as the initial condition of protostellar collapse. The degeneracy of temperature and column density that cannot be resolved with observations from the Rayleigh-Jeans regime only meant that this flattening was (under the assumption of isothermal spheres) naturally interpreted to originate in the density profiles.

External heating by the interstellar radiation field (ISRF) will, however, result in temperature profiles that decline toward the centre as the level of shielding by dust grains increases (e.g., Leung 1975). Evans et al. (2001) used radiative transfer calculations with ISRF heating to simulate spectral energy distributions (SEDs) for both isothermal cores and cores with temperature gradients. They find that the observed SEDs can also be explained with non-isothermal cores (see also Zucconi et al. 2001), which naturally results in smaller flat regions and enhanced central volume densities as compared to isothermal cores. In flux ratio maps of 170 and $200\,\mu\text{m}$, a wavelength range well outside the Rayleigh-Jeans regime for temperatures of the order of 10 K, Ward-Thompson et al. (2002) found observational evidence for such temperature gradients towards the centre of starless cores.

Knowledge of the temperature distribution throughout the molecular cloud cores is essential when it comes to understanding a few key processes in star formation, such as the appearance of molecules as a result of grain-surface chemistry (e.g., Taquet et al. 2013) or the excitation and radiation of gas-phase molecules (Pavlyuchenkov et al. 2007). Additionally, the thermal energy is the major contributor to the stability of a core

* The *Herschel* data (Fig. 2) including N- and T-maps in Fig. 3 are only available at the CDS via anonymous ftp to cdsarc.u-strasbg.fr (130.79.128.5) or via <http://cdsarc.u-strasbg.fr/viz-bin/qcat?J/A+A/569/A7>

against gravitational collapse (e.g., Launhardt et al. 2013). Low temperatures can promote gravitational instability in cores and inevitably lead – in the absence of other stabilising factors – to their collapse. During the early stage, these prestellar cores do show infall motions, but appear starless (e.g., Crapsi et al. 2005; Caselli et al. 2012). Once the central region with its enhanced density becomes opaque to infrared radiation, cooling becomes less efficient. Further compression is accompanied by a temperature rise, which leads to the formation of a so-called first hydrostatic core (FHSC; e.g., Larson 1969; Masunaga et al. 1998; Tomida et al. 2010; Commerçon et al. 2012) in a core, which is now of protostellar nature. Owing to their deeply embedded nature, low intrinsic luminosity, and short lifetime, FHSCs are hard to detect and still have to be unambiguously and observationally identified. Indeed, distinguishing these early phases of protostellar evolution has proven observationally challenging. Some FHSC candidates have been found so far (Belloche et al. 2006; Enoch et al. 2010; Chen et al. 2010, 2012; Pineda et al. 2011; Pezzuto et al. 2012), but none of these could be confirmed yet. Additional confusion for an unambiguous detection is caused by the fact that simulations of FHSC formation lead – depending on initial conditions and underlying physical processes – to different FHSC lifetimes, sizes, and luminosities, and this eventually leads to ambiguous predictions for observations (e.g., Omukai 2007; Masunaga et al. 1998; Saigo et al. 2008; Tomida et al. 2010; Commerçon et al. 2012). As Enoch et al. (2010) point out, the observational signature of a VeLLO (Very Low Luminosity Object, e.g., Young et al. 2004) could originate in either an FHSC or a highly embedded faint Class 0 protostar in a quiescent accretion phase (e.g., Stutz et al. 2013).

The launch of the *Herschel* Space Observatory¹ (Pilbratt et al. 2010) with its photometer wavelength coverage from 70 to $500\mu\text{m}$ allowed astronomers to view the earliest stages of star formation with unprecedented sensitivity and spatial resolution (e.g., Molinari et al. 2010; André et al. 2010; Stutz et al. 2010, 2013; Arzoumanian et al. 2011). The *Herschel* key programme EPoS (Earliest Phases of Star formation, PI: O. Krause) is dedicated to observations of both high-mass star-forming regions (e.g., Beuther et al. 2010, 2013; Henning et al. 2010; Linz et al. 2010; Ragan et al. 2012; Pitann et al. 2013; Kainulainen et al. 2013) and isolated low-mass pre- and protostellar cores (e.g., Stutz et al. 2010; Nielbock et al. 2012; Launhardt et al. 2013; Lippok et al. 2013). The focus for the low-mass part of the project is mainly on deriving the density and dust temperature structure in the early phases of protostellar evolution and on determining the initial conditions of protostellar collapse. Although most stars form in clustered environments (Lada & Lada 2003; Evans et al. 2009), the EPoS globule sample specifically focusses on nearby, isolated cores because they offer a pristine, undisturbed view of the basic processes that lead to the formation of protostars in the absence of complicating factors, such as competitive accretion, tidal interactions, and stellar feedback.

In this paper we present an observational study towards the EPoS target CB 17 (LDN 1389, Clemens & Barvainis 1988; Lynds 1962). This nearby, isolated Bok globule is located at an estimated distance of $250 \pm 50\text{ pc}$ and hosts a Class I protostar (IRS, accompanied by a near-infrared (NIR) nebula), and an adjacent dense core (SMM) at an angular separation of $\sim 30''$ or 5000 au (Launhardt et al. 2010). In sensitive 1.2 mm single-dish observations the emission around SMM exhibits a

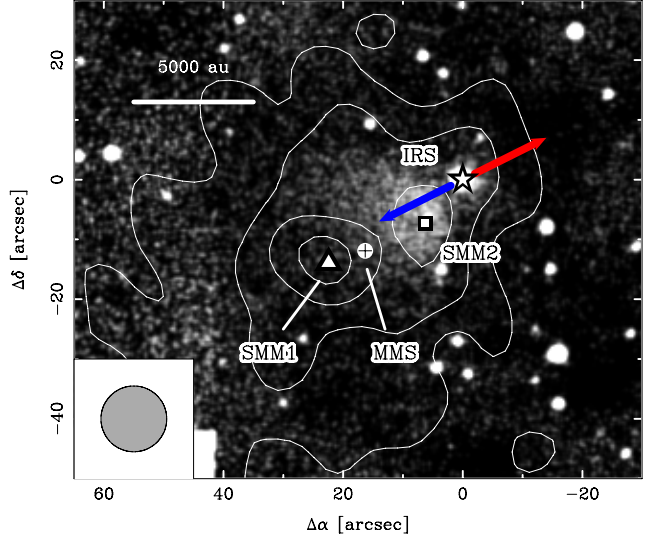


Fig. 1. 1.2 mm dust continuum emission (contours, plotted in steps of 3σ) overplotted on a NIR K image of CB 17 (Launhardt et al. 2010). The arrows represent the red- and blue-shifted components of the outflow detected by Chen et al. (2012). The grey circle in the bottom left corner represents the angular resolution of the 1.2 mm dust continuum image. The coordinate offsets are given w.r.t. to the position of IRS ($\alpha_{J2000} = 04^{\text{h}}04^{\text{m}}33\overset{\text{s}}{.}76$, $\delta_{J2000} = +56^{\circ}56'16\overset{\text{s}}{.}5$, Chen et al. 2012).

main peak (SMM1), but also shows a considerable extension towards the north-west (SMM2, see Fig. 1). Thanks to detections in all *Spitzer* MIPS bands and ground-based NIR observations, which allow a determination of the bolometric temperature (Launhardt et al. 2010), and the detection of low-velocity outflows (Chen et al. 2012), the classification of IRS is well established by now. In contrast, the evolutionary stage of SMM is still under debate. Detections of N_2H^+ (Caselli et al. 2002a) and NH_3 (Lemme et al. 1996), and a prominent $8\mu\text{m}$ -shadow at the position of strongest emission at mm-wavelengths (Launhardt et al. 2010) indicate that SMM has a starless nature. Recent studies by Launhardt et al. (2013) and Lippok et al. (2013) suggest that it is marginally bound and thus a prestellar core. In interferometric observations, Chen et al. (2012) detected a low S/N, compact 1.3 mm continuum source, MMS, within the boundaries of SMM (Fig. 1). Thanks to this detection in concert with a possible detection of a low-velocity outflow, Chen et al. (2012) classified MMS as a candidate FHSC, which would then mean that SMM is instead a protostellar core.

The goal of this paper is to perform an in-depth analysis of CB 17 and to reveal the evolutionary state of SMM. For this purpose we used far-infrared (FIR) *Herschel* dust emission maps (Launhardt et al. 2010; Lippok et al. 2013) and tailored our analysis to accommodate the morphological characteristics of CB 17. Moreover, we used interferometric observations of the cold gas-tracer N_2H^+ to spatially resolve the kinematic structure of the dense core.

This paper is structured as follows. In Sect. 2 we describe our observations and data. The temperature and density structure of CB 17, which is derived from the continuum data, is presented in Sect. 3. In Sect. 4 we focus on the small-scale structure and kinematics within the dense core. The findings from the two previous sections are then discussed in Sect. 5, which is followed by a summary in Sect. 6.

¹ *Herschel* is an ESA space observatory with science instruments provided by European-led Principal Investigator consortia and with important participation from NASA.

2. Observations

2.1. Dust continuum emission

2.1.1. Herschel

CB 17 was observed with SPIRE (Griffin et al. 2010) at 250, 350, and 500 μm and with PACS (Poglitsch et al. 2010) at 100 and 160 μm as part of the *Herschel* guaranteed time key programme EPoS on February 13 and 23, 2010, respectively. Observations with PACS were obtained with two scan directions oriented perpendicular to each other to eliminate striping in the final combined maps of effective size $\sim(11')^2$. The full width at half maximum (FWHM) beam sizes are 7.1'' at 100 μm and 11.2'' at 160 μm (Aniano et al. 2011). Likewise, the SPIRE observations were obtained as a scan map, covering an area of $\sim(18')^2$. The approximate FWHM beam sizes are 18.2, 25.0, and 36.4'' at 250, 350, and 500 μm , respectively (Aniano et al. 2011). A detailed description of these observations and the respective data reduction for all targets within the EPoS sample can be found in Launhardt et al. (2013).

2.1.2. Additional sub-mm observations

In addition to the *Herschel* observations, which cover the wavelength range from 100 to 500 μm , we used SCUBA observations at 850 μm (programme ID: M98BC21, beam size: 14.3'') and IRAM 30 m continuum observations at 1.2 mm (beam size: 10.9''). A detailed overview of these observations can be found in Launhardt et al. (2010, 2013).

2.2. Molecular line emission

Complementary to the observations of thermal dust emission with *Herschel*, we also observed line radiation from N₂H⁺. This molecule is known to be a tracer of the structure and kinematics of dense cores (Johnstone et al. 2010). This is mainly because CO as a C-bearing molecule that can destroy N₂H⁺ freezes out onto the dust grains in the cold dense cores, whereas N-bearing molecules are less prone to this effect. Furthermore, with its critical density of $n_{\text{H},\text{crit}} \sim 10^5 \text{ cm}^{-3}$, N₂H⁺(1–0) emits most strongly at the densities that are reached in low-mass prestellar cores (Launhardt et al. 2010).

Observations of the N₂H⁺(1–0) hyperfine structure (HFS) complex at 93.171 GHz were obtained with the Plateau de Bure Interferometer (PdBI) on 2 and 8 April 2009 in configurations 6Cq and 6Dq, respectively. 3C84 served as bandpass and flux density calibrator, and 0444+634 and 0355+508 served as gain calibrators. The spectrometer was set up to have a bandwidth of 20 MHz, with each of its 512 channels having a width of 39 kHz. At the frequency of the N₂H⁺(1–0) transition, the total bandwidth then conforms to a velocity range of 64 km s⁻¹ and a channel separation of 0.13 km s⁻¹ (and thus an effective spectral resolution of 0.24 km s⁻¹). Therefore, we were easily able to capture the full extent of the HFS complex, which stretches out over 15 km s⁻¹.

In addition to the interferometric observations, we used single-dish data to account for the missing short spacings. This data was obtained with the IRAM-30 m antenna with OTF mapping on 12 July 2004. The data is remapped to match the phase centre of the PdBI observations, and then merged with the interferometric data. Calibration, combination of single-dish with interferometric data, imaging, and image deconvolution are all

performed by using GILDAS² software. Natural weighting of the *uv*-data results in a synthesised FWHM beam size of 4.5'' \times 3.7'' and a sensitivity of 10 mJy beam⁻¹ per channel.

3. Large scale temperature and density distribution

3.1. Overview

The *Herschel* observations, which are shown in Fig. 2, give an overview of the thermal dust emission of CB 17. The bulk of the emission is found around SMM and IRS. A long cometary tail extending towards the north-east can easily be seen at all wavelengths $>100 \mu\text{m}$. The 160 μm image shows a set of bright knots of emission along this tail, a feature that is washed out with increasing wavelength owing to the decreasing spatial resolution.

The detailed views in Fig. 2 show that the Class I protostar IRS is the dominant source at wavelengths shorter than 200 μm , whereas at longer wavelengths the bulk of the emission comes from the dense core SMM. This shift in the emission peak with wavelength has also been observed in CB 244, which hosts a Class 0 protostar and a pre-stellar core at an angular separation of $\sim 100''$ (Stutz et al. 2010). It can be clearly attributed to the different evolutionary stages. Spectral energy distributions of protostellar cores are, compared to starless cores, characterised by higher temperatures, which results in a shift of the emission peak towards shorter wavelengths. In CB 17, this effect is less clear because of the small angular separation between IRS and SMM, which leads to considerable blending of the emission from these two sources.

3.2. Dust temperature and hydrogen volume density profiles

In the pre-*Herschel* era, dust emission was often used to estimate column densities and masses through single-wavelength observations, using an educated guess for the dust temperature and dust opacity (e.g., Launhardt & Henning 1997; Motte et al. 1998). With *Herschel* it is possible to use both the spectral and spatial information of the dust continuum emission to model the density and dust temperature distribution. For our modelling, the available *Herschel* observations were complemented by SCUBA and IRAM 30 m data, which extends the wavelength coverage from 100 μm to 1.2 mm. Thus, we fully sample the peak of the SED.

To determine the dust temperature and hydrogen volume density profiles, we closely follow the procedures as described in Launhardt et al. (2013) and Lippok et al. (2013). We use dust opacities from Ossenkopf & Henning (1994) for coagulated dust with thin ice mantles (0.1 Myr of coagulation time at a gas density of 10^5 cm^{-3}) and a hydrogen gas-to-dust mass ratio of 110 (Sodroski et al. 1997). In contrast to previous studies by Launhardt et al. (2013) and Lippok et al. (2013), which also included CB 17, we are deliberately omitting the observations at 500 μm to gain a factor of 1.5 in terms of spatial resolution. All our images are then convolved to the *Herschel* beam of 350 μm (25'' or 6 250 au). This allows us to reduce the blending of the emission from the dense core and the Class I source. Moreover, by using a higher spatial resolution we aim to minimise convolution effects for a bona fide determination of a flattening of the volume density profile towards the centre.

To determine the temperature, column, and volume density structure of CB 17, we apply two different techniques. The modified blackbody (MBB) routine gives us line-of-sight

² <http://www.iram.fr/IRAMFR/GILDAS/>

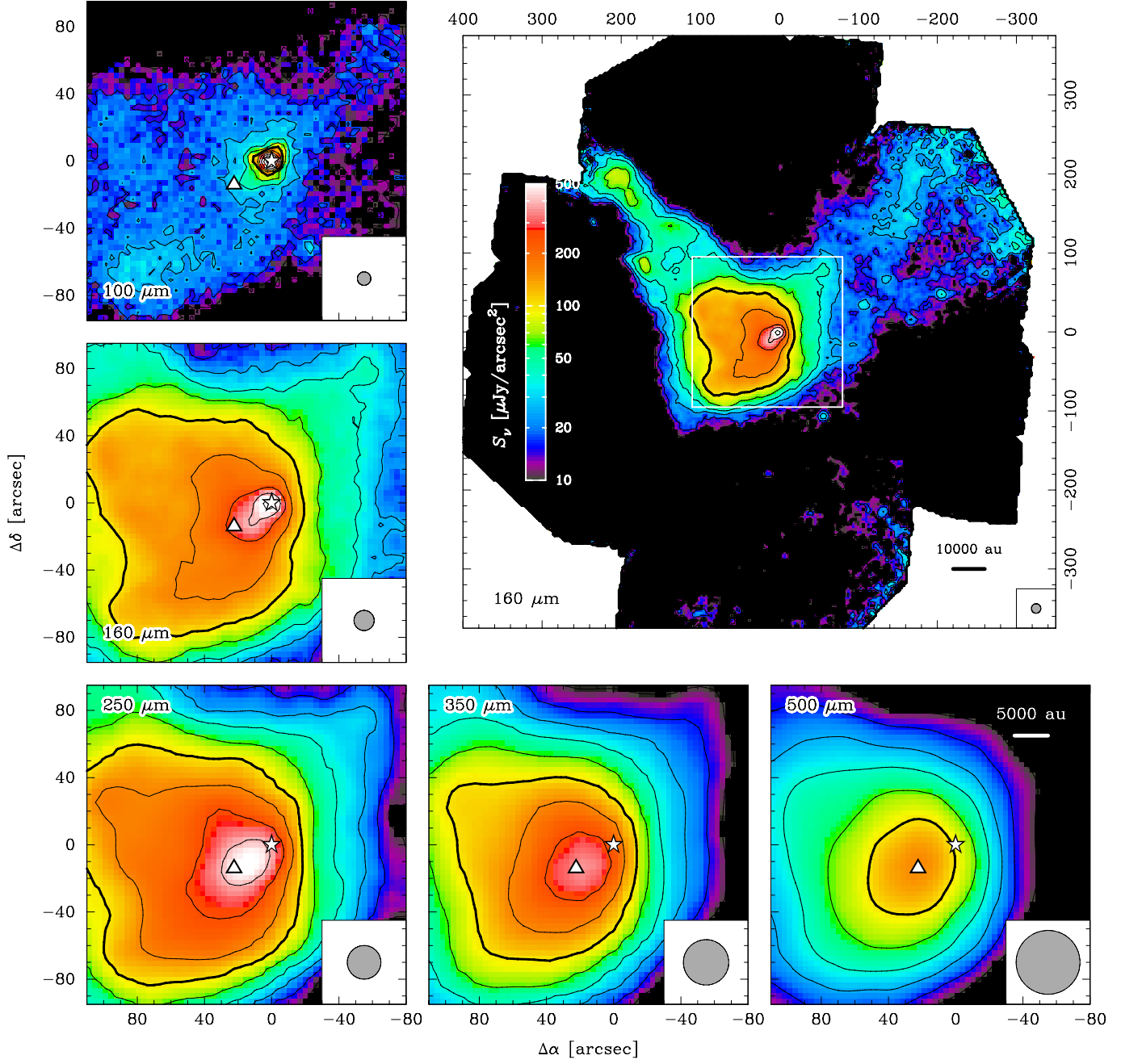


Fig. 2. *Herschel* dust emission maps at 100 μm, 160 μm, 250 μm, 350 μm, and 500 μm. The big panel represents the full field of view at 160 μm, which shows the cometary structure of CB 17. The small panels show detailed views of the white rectangular area for all *Herschel* observations, ranging from 100 μm to 500 μm. The surface brightness scale is the same for all images. The contours range from 10 μJy/arcsec² up in logarithmic steps of 0.2 dex. The thick contour represents 100 μJy/arcsec². The respective beam sizes are depicted in the bottom right corners. Symbols mark the positions of SMM1 (\blacktriangle) and IRS (\star).

averaged quantities, whereas the ray-tracing (RT) approach accounts for temperature and volume density gradients along the line-of-sight. The radial temperature profile in the RT-model is defined as

$$T(r) = T_{\text{core}} - \Delta T \left(1 - e^{-\tau_{\text{ISRF}}(r)}\right) \quad (1)$$

where $\Delta T = T_{\text{core}} - T_{\text{min}}$. T_{core} represents the temperature at the core edge, and T_{min} is the minimum temperature. The term

$$\tau_{\text{ISRF}}(r) = \tau_{\text{ISRF},0} \frac{\int_r^{r_{\text{core}}} n_{\text{H}}(r') dr'}{\int_0^{r_{\text{core}}} n_{\text{H}}(r') dr'} \quad (2)$$

accounts for the a priori unknown mean dust opacity and the UV shape of the ISRF, where $\tau_{\text{ISRF},0}$ is an empirical scaling parameter. The temperature in the core centre T_0 is then calculated by

$$T_0 = T_{\text{core}} - \Delta T \left(1 - e^{-\tau_{\text{ISRF},0}}\right), \quad (3)$$

which converges towards T_{min} for $\tau_{\text{ISRF},0} \gg 1$.

In our analysis, the hydrogen volume density profile is defined as

$$n_{\text{H}}(r) = \frac{n_{\text{H},0}}{[1 + (r/r_0)^2]^{\eta/2}} \quad (4)$$

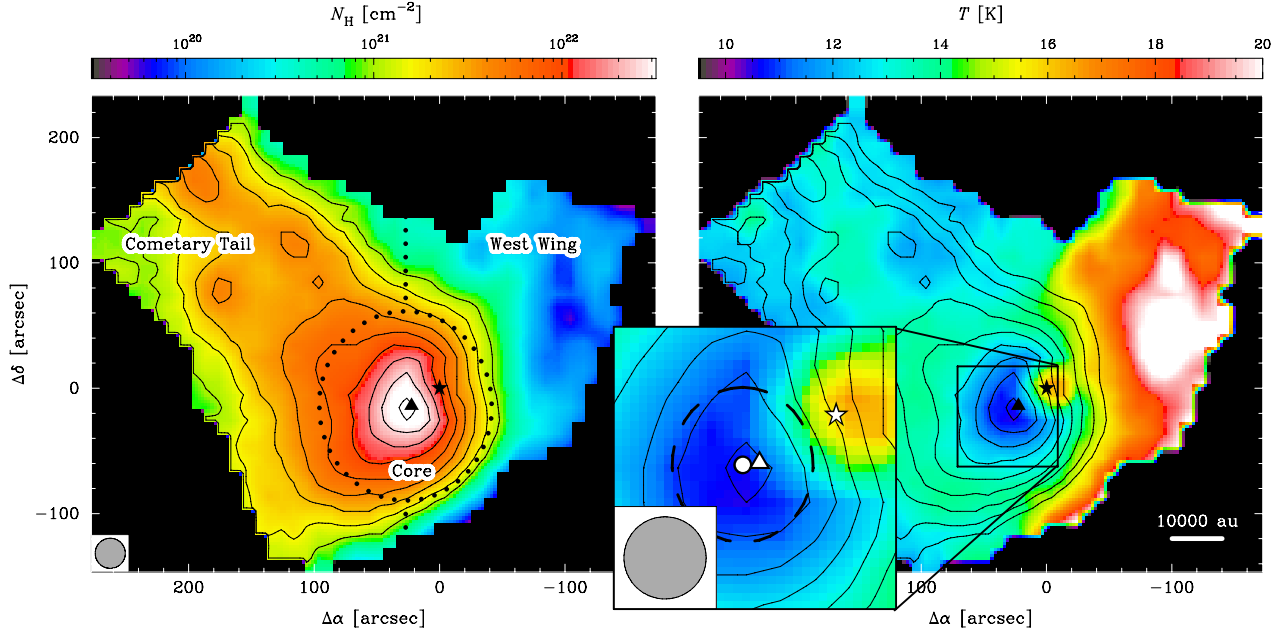


Fig. 3. Hydrogen column density (left panel) and dust temperature maps (right panel) of CB 17. The dotted lines mark the boundaries between the three regions discussed in the text (core, cometary tail, west wing). The data for the cometary tail and west wing are fitted by using the MBB algorithm, whereas the core is fitted using the RT-procedure (Sect. 3.2). The temperature in the core represents the mid-plane temperature (i.e., the minimum temperature along the line-of-sight), whereas in the other two regions the LoS-averaged dust temperature is displayed. Symbols mark the positions of SMM1 (\blacktriangle) and IRS (\star) from Launhardt et al. (2010). The inset shows a zoom towards the cold and dense regions. The newly derived position of SMM1 and the FWHM of the volume density distribution are marked with a white circle and dashed line, respectively. The contours in all panels represent the column density, starting from $N_{\text{H}} = 10^{21} \text{ cm}^{-2}$, and subsequent levels in steps of 0.2 dex.

where $n_{\text{H},0}$ is the density of hydrogen nuclei in the core centre, r_0 is the radius of the central density plateau, and η the power-law slope at large radii. We cut off the density profile at a radius of $r_{\text{out}} = 30\,000 \text{ au}$ at volume densities of a few 10^2 cm^{-3} . The value of r_{out} is unconstrained, but setting a cutoff at larger radii only has a marginal effect on the best-fit parameters.

The hydrogen column density and temperature maps are shown in Fig. 3. Towards the regions of highest density (Core) we applied the RT approach. Owing to the apparent breakdown of spherical symmetry at $r \gtrsim 18\,000 \text{ au}$ (which can be seen in the radial profiles discussed later in this paragraph), the map shows the line-of-sight averaged quantities from the MBB fitting outside the core. That no jumps are seen in temperature or column density at the transition between the core (RT) and envelope (MBB) confirms that temperature gradients are only important within the core region and that the MBB approximation is therefore appropriate for the envelope.

The column density peak, which is also accompanied by a temperature minimum, is obviously offset from IRS. We see no indication of a local column density enhancement at the position of the Class I source, which suggests that it is not deeply embedded, but most likely located in front of or behind the dense core, and devoid of significant amounts of circumstellar material. We attribute the offset between the position of IRS and the temperature peak as being the result of blending the emission of the cold, dense core with the Class I source (see inset in Fig. 3). This could also compromise determination of the position of the dense core, which is defined as the column-density weighted mean position. We estimated a positional uncertainty of the dense core to be of the order of $10''$. Despite this uncertainty, the position of the column density peak and temperature minimum are spatially coeval with the emission peak SMM1 in the 1.2 mm continuum (Launhardt et al. 2010). Henceforth, we denote the dense core as SMM1.

The radial dust temperature and hydrogen volume density profiles of SMM1 are shown in Fig. 4, and the best-fit parameters are listed in Table 1. The breakdown of the spherical symmetry is particularly obvious in these plots. We separate CB 17 into three distinct regions: the core, the warm west wing, and the cometary tail (see Fig. 3).

The dense core SMM1 is characterised by a flat inner plateau with $r_0 \sim 9500 \text{ au}$ and a power-law index of $\eta = 4.9$, which conforms to a FWHM of the core volume density distribution of $10\,900 \text{ au}$. Since this is well beyond the spatial resolution ($\sim 6000 \text{ au}$), we conclude that the flattening towards the centre is not an artefact of the image convolution. This indicates an early evolutionary stage, since a flat volume density profile is characteristic of prestellar cores, whereas protostellar cores exhibit power-law density distributions down to radii well below our resolution limit (e.g. Jørgensen et al. 2002). The central volume density is derived to be $n_{\text{H}} = 2.3 \times 10^5 \text{ cm}^{-3}$. In contrast to Lippok et al. (2013), we derive by a factor of ~ 1.5 higher column and volume densities, and a slightly smaller plateau radius. These differences can be attributed entirely to the different spatial resolutions that were used in these two studies.

The derived parameters and error bars assume the single dust model that we used in this paper. An analysis and discussion of how different dust models might affect the derived parameters can be found in Launhardt et al. (2013) and Lippok et al. (2013).

4. A high-resolution view of SMM1

4.1. Dust continuum emission

Among our available FIR data, the $100 \mu\text{m}$ map offers the highest spatial resolution, which is beneficial for disentangling the emission of the Class I source IRS and a potential emission contribution from an embedded source in SMM1. In the original

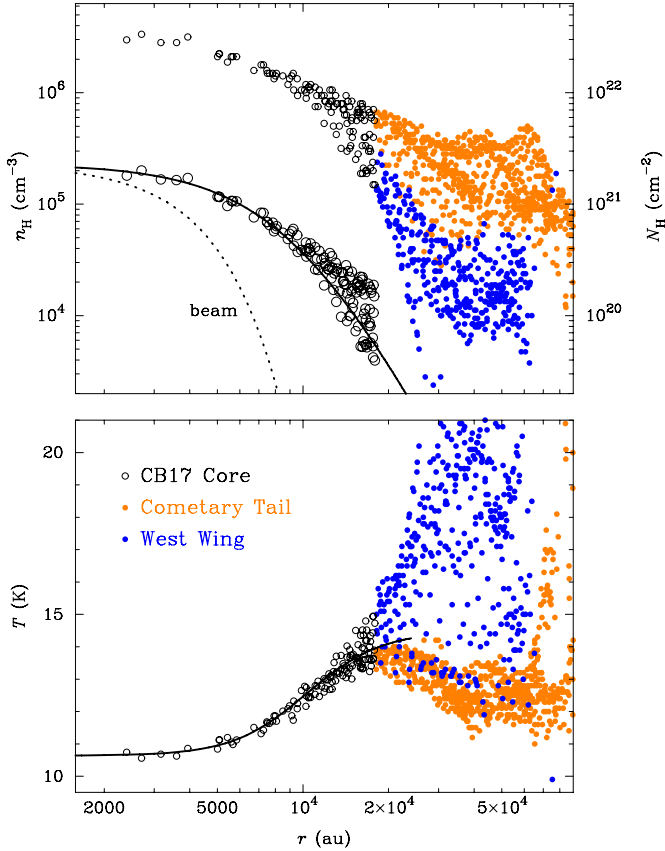


Fig. 4. Azimuthally averaged column density (top, small symbols), volume density (top, large symbols), and temperature (bottom) distributions. The data for the cometary tail and the west wing are taken from the MBB, whereas the data for the core is the result of the RT fit (Sect. 3.2). The pixels within a beam size from the Class I protostar IRS are excluded. The solid line shows the curves for the best-fit model (Table 1), the dotted line indicates the beam size.

Table 1. CB 17-SMM1 dense core parameters.

LoS-averaged fit parameters [†]	
α_0 (J2000)	$04^\circ 04' 37.1 \pm 10''$
δ_0 (J2000)	$+56^\circ 56' 02'' \pm 10''$
aspect ratio	1.1
PA	179°
r_{out}	30×10^3 au
r_{core}	18×10^3 au
T_{core}	14.2 ± 0.7 K
ray-tracing fit parameters [‡]	
r_0	$(9.5 \pm 0.6) \times 10^3$ au
η	4.9 ± 0.4
$\tau_{\text{ISRF},0}$	6.5 ± 0.7
T_0	10.6 ± 0.3 K
$n_{\text{H},0}$	$(2.3 \pm 0.2) \times 10^5$ cm $^{-3}$
$N_{\text{H},0}$	$(4.3 \pm 0.2) \times 10^{22}$ cm $^{-2}$
M_{core}	$(2.3 \pm 0.3) M_\odot$

Notes. ^(†) These parameters are derived from the column density and dust temperature map derived through the LoS-averaged fitting, and are kept constant during the ray-tracing fitting. ^(‡) These parameters are derived from the azimuthally averaged mid-plane volume density and dust temperature profiles (Fig. 4) after each iteration cycle. The error bars are only representative of the used dust model. A more general discussion about how different dust models influence the best-fit parameters can be found in Lippok et al. (2013).

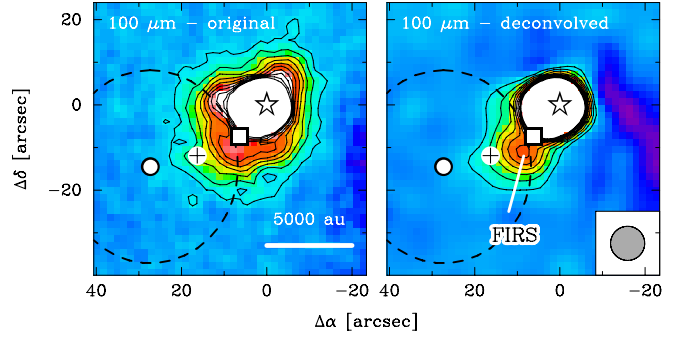


Fig. 5. Original (left) and deconvolved (right panel) 100 μm images. The colour scales are exaggerated to highlight the presence of the faint emission feature FIRS. The symbols mark the positions of SMM1 (●), IRS (★), SMM2 (■), and the FHSC candidate MMS (+). The dashed line marks the FWHM of the SMM1 volume density distribution. In both images, the contours are plotted in steps of 3σ above the level of the background cloud. (This noise does not necessarily represent the true noise level around the protostar.) The beam size of the 100 μm observations is indicated in the bottom right corner.

100 μm map, additional faint emission close to the dominating signal from the Class I source is apparent, but is confused by the non-trivial structure of the PACS point-spread function (PSF). We therefore deconvolve the 100 μm map to obtain a clearer view of IRS and its immediate surroundings.

In Chen et al. (2012; hereafter referred to as CAD12), we show a preliminary analysis where the *Herschel* 100 μm data was reduced using Scanamorphos v9.0 (Roussel 2013) and the nothermal, noglitch, and galactic options. For the deconvolution, which was performed with the miriad task CLEAN, the azimuthally averaged *Herschel* PSF at 100 μm (Aniano et al. 2011) was taken. This treatment of the data indicated a faint, slightly extended 100 μm emission source at a distance of $\sim 20''$ to the south-east of IRS with a flux density of 36 ± 2 mJy (see Fig. 2b and Table 4 of Chen et al. 2012). The secondary *Herschel* source appeared to be spatially coincident with the compact 1.3 mm continuum source, MMS. Its SED – including the 100 μm source – agreed with classifying it as a FHSC candidate embedded in the prestellar core SMM1.

Here we reiterate the nature of this faint 100 μm source – hereafter called CB 17-FIRS. We performed a more thorough analysis, using the latest data reduction version (Scanamorphos v18.0; nothermal and galactic options), together with the appropriate 100 μm PACS PSF ($20''$ s $^{-1}$ scan speed, not re-centred, no enhanced drizzling), derived from observations of the asteroid Vesta and provided by the PACS instrument team³. Before the deconvolution, the PSF was rotated counter-clockwise by 260.45° in order to match the orientation of the PSF present in the CB 17 PACS observations. We applied five iterations of a modified Richardson-Lucy deconvolution (Richardson 1972; Lucy 1974) as implemented in IDL.

In the resulting deconvolved map, we confirm the presence of a secondary emission patch, which is clearly distinguishable from the emission of the Class I source (Fig. 5). This improved analysis results in a positional shift of FIRS by $7''$ towards the west, as compared to the preliminary analysis reported in CAD12. The reason for this is two-fold. First, the new data reduction shows a slightly different emission structure in the immediate vicinity of IRS. The weak emission, which is clearly

³ ftp://ftp.sciops.esa.int/pub/hsc-calibration/PACS/PSF/PACSPSF_PICC-ME-TN-033_v2.0.tar.gz

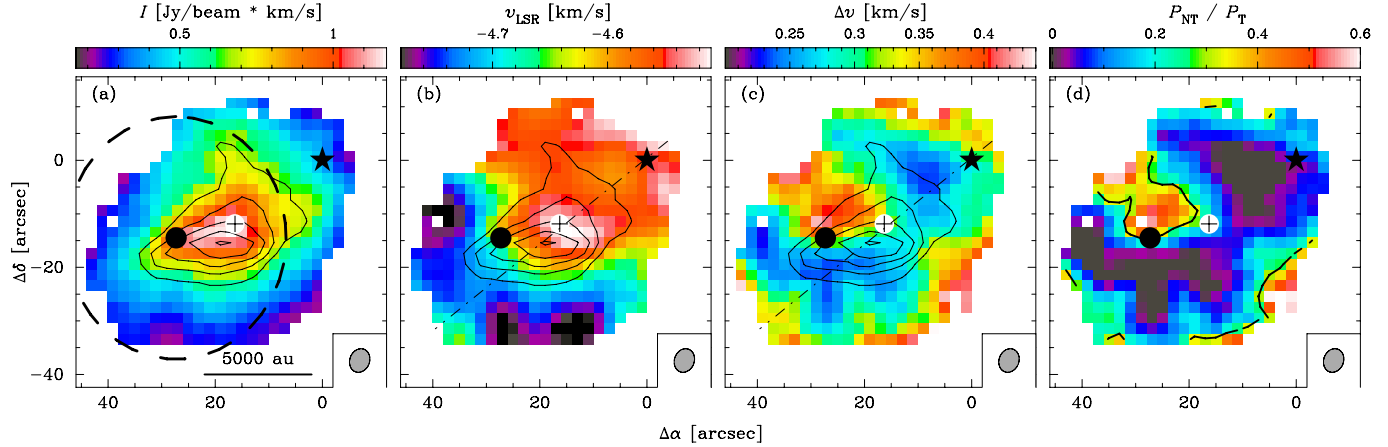


Fig. 6. From left to right: N_2H^+ maps of integrated intensity, velocity centroid, linewidth, and ratio of non-thermal to thermal pressure. Symbols mark the positions of SMM1 (●), MMS (+), and IRS (★). The dashed circle in panel **a**) represents the FWHM volume density distribution of SMM1. The contours in panels **a**–**c**) represent the N_2H^+ column density with contours from $(1 \dots 3) \times 10^{13} \text{ cm}^{-2}$ in steps of $0.5 \times 10^{13} \text{ cm}^{-2}$. In panel **d**) the contour marks the $P_{\text{NT}}/P_{\text{T}} = 0.3$ line. The dash-dotted lines in panels **b**) and **c**) mark the cut for the position-velocity diagram, which is shown in Fig. 7. The synthesised beam size is indicated in the bottom right corners.

visible in the original images (Fig. 2), is found further away from the Class I protostar in the early data reduction. Second, the use of the properly structured and oriented PSF instead of the azimuthally averaged PSF approximation minimises residual emission features from the bright source IRS, which can be mistaken as true emission features from the faint source FIRS. This unfavourable morphology makes both the data calibration and the image deconvolution challenging and introduces uncertainties for position and flux density beyond the level we would experience for an isolated source.

In contrast to its position, the determined flux density and size of FIRS remained unchanged with respect to the preliminary analysis. Owing to the proximity of IRS, the size and flux density are estimated by fitting 1D Gaussian profiles along north-east and south-west directions. We determine a FWHM of $11.3''$ (which is considerably larger than the beam size of $\sim 7.1''$) and a flux density of 35 mJy . Considering the difficulties, which were discussed in the previous paragraph, we assume that the flux density is not known better than to a factor of 2. However, according to our current analysis, we assume that we can determine the position of FIRS fairly reliably. The implications of this newly derived position on the FHSC candidate MMS is discussed in Sect. 5.3.

4.2. Kinematics of the dense core SMM1

To analyse the kinematics of the dense core SMM1, we obtained complementary observations of $\text{N}_2\text{H}^+(1-0)$ with an angular resolution of $\sim 4''$. The hyperfine structure complex offers the big advantage of providing a multitude of parameters, such as optical depth, τ , or excitation temperature, T_{ex} , with a single observation, for which usually observations of optically thin and thick isotopes would be necessary. Furthermore, the simultaneous fit of all HFS satellites allows determination of the systemic velocity v_{LSR} and line FWHM Δv with much higher precision than for a single line, even for data with moderate-to-low S/N. Lippok et al. (2013) use single-dish observations of N_2H^+ in concert with CO data to determine molecular abundance profiles and gas-phase depletion in CB 17 and other starless cores of the EPoS-sample, but they do not spatially resolve the kinematic structure as we attempt to do here.

For the fitting, we used the hyperfine structure fitting routine provided by CLASS, which is a part of the software package GILDAS. The transition frequencies and relative weights of the HFS lines were taken from Caselli et al. (1995); Womack et al. (1992), respectively. For the fit we only included spectra, where the isolated HFS component ($F_1 F = 01 \rightarrow 12$) exhibited a peak value of $\geq 5\sigma$.

The spectrum towards the column density peak of N_2H^+ exhibits a total optical depth, i.e., the sum of the optical depths of the individual HFS components, of $\tau = 25$, an excitation temperature of $T_{\text{ex}} = 7.5 \pm 0.3 \text{ K}$, and a peak column density of $N(\text{N}_2\text{H}^+) = 3.6 \times 10^{13} \text{ cm}^{-2}$. Maps of the fitted N_2H^+ integrated line intensity I , the velocity centroid v_{LSR} , linewidth Δv , and column density $N(\text{N}_2\text{H}^+)$ are shown in Fig. 6. Additionally, we plot the ratio of thermal to non-thermal pressure (Tafalla et al. 2004)

$$\frac{P_{\text{NT}}}{P_{\text{T}}} = \frac{\Delta v_{\text{NT}}^2}{\sqrt{8 \log(2)}} \frac{\mu_p m_H}{k_B T}, \quad (5)$$

where $\mu_p = 2.32$ is the mean atomic mass per particle in molecular clouds (Przybilla et al. 2008). The temperature was taken from the RT fit (Sect. 3.2), because we assumed the gas and dust to be well-coupled in the centre at densities $n_H \sim 2 \times 10^5 \text{ cm}^{-3}$. The non-thermal linewidth was derived by

$$\Delta v_{\text{NT}} = \sqrt{\Delta v^2 - (\Delta v_{\text{T}}^2 + \Delta v_{\text{instr}}^2)}, \quad (6)$$

where Δv is the measured linewidth, Δv_{T} the thermal linewidth, and $\Delta v_{\text{instr}} = 0.235 \text{ km s}^{-1}$ is the instrumental resolution (which is 1.875 times the channel spacing).

Clearly, $\text{N}_2\text{H}^+(1-0)$ emission is only coming from within SMM1, whereas no emission comes from IRS (Fig. 6a). The position of the column density peak of N_2H^+ can be associated with MMS, which is offset from the centre of SMM1. This could be due to substructure in the densest part, which can be traced by interferometric molecular line observations, but remains undetected by the large-scale dust emission at five times lower spatial resolution. The N_2H^+ column density distribution can be approximated by an elliptical Gaussian with major and minor axes (FWHM) of 7100 au and 5900 au , respectively. The major axis exhibits a PA = 135° (East of North).

We derive a N_2H^+ peak column density that is about ten times higher than the value determined by Caselli et al. (2002a). Their low spatial resolution, however, leads to considerable beam dilution, which then underestimates the excitation temperature, optical depth, and thus the column density. From fitting the IRAM 30 m single-dish spectra alone, we determine an optical depth of $\tau \sim 9$ and $T_{\text{ex}} \sim 5$ K, which agrees with the observations of Caselli et al. (2002a). To assess whether our interferometric observations of N_2H^+ also suffer from beam dilution effects, we estimated the expected excitation temperature T_{ex} with the on-line tool RADEX (van der Tak et al. 2007). We used the best-fit dust temperature T_0 , as well as the N_2H^+ column density and linewidth, as input parameters. The observed value of $T_{\text{ex}} = 7.5$ K would be reached at a density of $n_{\text{H}} \sim 3 \times 10^5 \text{ cm}^{-3}$, which is in good agreement with our finding of the central density of $n_{\text{H},0} = 2.3 \times 10^5 \text{ cm}^{-3}$, taking the uncertainties introduced by the dust model into account. This analysis indicates that the 25'' resolution of Herschel observations is sufficient to accurately sample the structure of the core on the scales of the dense core plateau. This in turn allows us to obtain a robust estimate of the central volume density.

The velocity map (Fig. 6b) shows a clear gradient from south-east towards north-west of $\sim 4.3 \pm 0.2 \text{ km s}^{-1} \text{ pc}^{-1}$ (following the recipe of Kane & Clemens 1997). In addition to the large-scale velocity gradient, which we attribute to rotation of the core around an axis with PA = $54 \pm 2^\circ$, the velocity map also exhibits a complex small-scale structure, which is discussed in more detail in Sect. 5.2.2.

Similar to the velocity profile, the linewidth map (Fig. 6c) also reveals complex structure. Large parts of the dense core exhibit a relatively constant line width of the order of $\Delta v \sim 0.25 \text{ km s}^{-1}$. Figure 6d shows that non-thermal contributions in some parts of the cloud are negligible. We furthermore see no evidence of any infall motions, which would reveal themselves through increased linewidth towards the centre (Caselli et al. 2002b) and – in case of excitation gradients along the line of sight in concert with optical depths above unity – asymmetric, self-absorbed line profiles (Crapsi et al. 2005). This is consistent with Pavlyuchenkov et al. (2006), who finds only weak infall motions in the envelope. On the other hand, N_2H^+ freeze-out towards the core centre could inhibit the appearance of infall signatures due to the absence of gas phase molecules in that region (Lippok et al. 2013).

The only region with considerably elevated linewidths is a cone-shaped region that opens up towards the north-east. We find a ratio of non-thermal to thermal pressure $P_{\text{NT}}/P_{\text{T}} > 0.3$ (Fig. 6d) in this region. We do not attribute the increased linewidth to being caused by infall motions due to the lack of spherical symmetry.

5. Discussion

5.1. A large-scale overview

In Sect. 3.2, we determine the temperature and column density distribution of CB 17 via MBB and RT fitting (Fig. 3). The cometary shape of the globule stands out clearly. The column densities in the cometary tail towards the north-east are about ten times lower than the peak column density of the core. Interestingly, towards the north-west we see a warm west wing, where the dust temperatures are $\gtrsim 20$ K and hydrogen column densities are as low as $\sim 10^{19} \text{ cm}^{-2}$. As discussed earlier, the specific morphology of CB17 and the low envelope temperature (as compared to most other globules) prevent us from

deriving reliable values for the extended envelope levels of both the temperature and column density.

In the cometary tail we already reach our sensitivity limits at column densities of the order of $N_{\text{H}} \sim 3 \times 10^{20} \text{ cm}^{-2}$, hence more than a magnitude higher than the west wing. This is due to the lower temperatures and thus the lower emission levels. The west wing might be part of a warm background/foreground cloud or filament that is seen in the large-scale $160 \mu\text{m}$ map in Fig. 2. Whether this region is physically connected to CB 17 is not clear. An answer to this question could be provided by molecular line data that traces the kinematics across the boundary, which we do not have at hand.

5.2. Characterising SMM1

5.2.1. Energy balance

Starless and prestellar cores are the best probes for a ray-tracing fitting analysis as introduced in Sect. 3.2 thanks to their relatively simple temperature and volume density structure. Knowing the temperature and density profiles allows us to perform a stability analysis of the dense core SMM1 at an unprecedented level of accuracy. Using the equations listed in Appendix A, we find a gravitational potential energy of $E_{\text{grav}} = -(4.2 \pm 1.0) \times 10^{35} \text{ J}$, a thermal energy of $E_{\text{therm}} = (3.0 \pm 0.5) \times 10^{35} \text{ J}$, a turbulent energy of $E_{\text{turb}} = (2.3 \pm 0.4) \times 10^{34} \text{ J}$ (where we estimated an average non-thermal linewidth of $\Delta v_{\text{NT}} = 0.2 \text{ km s}^{-1}$), and a rotational energy of $E_{\text{rot}} = (6.3 \pm 1.8) \times 10^{34} \text{ J}$ within the central 18 000 au.

Using the results from above we also assess the stability of SMM1 by comparing the various energy components. Thanks to the availability of kinematic information, we are not limited to comparing gravitational potential and thermal energies (e.g. Lippok et al. 2013). By neglecting the contribution from magnetic fields for the moment, the criterion for a core to be bound is

$$\frac{E_{\text{therm}} + E_{\text{turb}} + E_{\text{rot}}}{|E_{\text{grav}}|} \leq 1. \quad (7)$$

Integration of the density and temperature distribution from inside out shows that this ratio is $\gg 1$ at small radii, reaches unity at $r \sim 8000$ au, and converges towards 0.93 ± 0.10 at r_{core} . This means that the core is literally on the margin of being bound at the scale of the core size. Pavlyuchenkov et al. (2006) find a chemical age of the envelope of CB 17 of 2 Myr, which is five times its free-fall time. Therefore, these authors conclude that CB 17 must have evolved quasi-statically for some time, which agrees with our result of a globule on the verge of being bound – neither collapsing nor dispersing.

This picture will also not change when including magnetic fields. An attempt to measure the degree of polarisation, hence the magnetic field strength in CB 17, has been undertaken by Matthews et al. (2009). Although we are not able to get a statistically significant estimate of the magnetic field with only two polarisation vectors, we can use these observations to estimate an upper limit of the order of $10 \mu\text{G}$, and consequently a magnetic energy of the order of $E_{\text{mag}} \lesssim 3 \times 10^{34} \text{ J}$. Therefore, the influence of magnetic fields on the stability of CB 17 is considered to be insignificant.

Using the LoS-averaged column density and temperature maps results in over-predicting the thermal energy by a factor of 1.3. In addition, the LoS-averaged column density map does not yield a direct handle on the value of the gravitational potential $E_{\text{grav}} = \alpha_{\text{vir}} GM_{\text{core}}^2/r_{\text{core}}$, since the pre-factor α_{vir} depends on the radial volume density distribution of mass. Thus, the ray-tracing

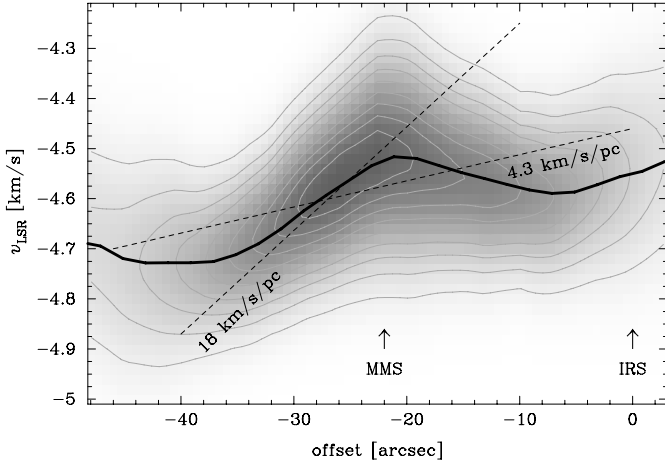


Fig. 7. Position-velocity diagram for $\text{N}_2\text{H}^+(1-0)$ along the cut marked in Figs. 6b,c from south-east to north-west. The solid line marks the fitted velocity to highlight the shape of the curve. Contours are plotted in steps of 10% of the peak emission. The two dashed lines indicate (a) the velocity gradient attributed to solid body rotation of the core (with a measured slope of $4.3 \text{ km s}^{-1} \text{ pc}^{-1}$); and (b) the CAD12 $\text{N}_2\text{D}^+(3-2)$ gradient of $18 \text{ km s}^{-1} \text{ pc}^{-1}$ for comparison. See Sect. 5.2.2 for more details.

allows us to significantly reduce the uncertainties in our parameter estimates, greatly improving the ability to assess the energy balance of SMM1. Moreover, including the information about kinematics (turbulence plus rotation) allows us to get a more reliable estimate of the core state, since its contribution is about 30% of the thermal energy. Simply neglecting it would lead to the conclusion that SMM1 is indeed bound.

5.2.2. Velocity structure

Inspection of the velocity map (Fig. 6b) already reveals a high level of complexity. Fitting the large-scale velocity distribution reveals a gradient of $4.3 \text{ km s}^{-1} \text{ pc}^{-1}$ from south-east to north-west. This is superposed by a sinusoidal pattern with a peak-to-peak amplitude of $\sim 0.15 \text{ km s}^{-1}$ (Fig. 7). We interpret this velocity structure as being the result of the superposition of two types of motion: SMM1 exhibits solid-body rotation on a large scale, but the inner regions are characterised by differential motions with respect to the dense core. In this scenario, the blue-shifted material with respect to the dense N_2H^+ knot represents the outer layers that get stripped off due to the differential motion, which is $\sim 0.2 \text{ km s}^{-1}$. In their survey of 42 isolated cores, Walsh et al. (2004) find only small velocity differences $\lesssim 0.1 \text{ km s}^{-1}$ between N_2H^+ cores and envelopes (traced by ^{13}CO and C^{18}O). For CB 17, these authors find a velocity difference of $\sim 0.1 \text{ km s}^{-1}$ between N_2H^+ and C^{18}O , whereas ^{13}CO and N_2H^+ are at about the same velocity. However, their low spatial resolution of $\sim 50''$ does not allow them to resolve the small-scale structure of this source. An additional complication comes from the fact that CB 17 has fragmented into at least two sources. It could be that the motion of the N_2H^+ knot within the dense core is part of an orbital motion with IRS. We have no means to quantify that assumption, but from the observations of molecular lines at hand, we can assume an upper limit of the relative radial velocities of 0.2 km s^{-1} , which is a value that does not contradict what can be expected for the orbital motion of two bodies with a few solar masses at a separation of the order of 10^4 au .

The observed overall velocity gradient of $4.3 \text{ km s}^{-1} \text{ pc}^{-1}$ agrees with what is generally found for prestellar cores

(Caselli et al. 2002a), whereas Class 0 sources rotate an order of magnitude faster (Chen et al. 2007). In their observations of $\text{N}_2\text{D}^+(3-2)$, CAD12 derived a velocity gradient of $18 \text{ km s}^{-1} \text{ pc}^{-1}$, which led to the conclusion that SMM1 should already be a rather evolved core and might have formed a FHSC, MMS, in the centre. However, $\text{N}_2\text{D}^+(3-2)$ is only observed (due to missing short spacings in the interferometric observations, molecular abundance, and/or excitation conditions) in a region to the south-east of the N_2H^+ column density peak. This region translates into offsets between -35 and $-20''$ in the position-velocity cut (Fig. 7), where the velocity profile of N_2H^+ is also rather steep. Therefore, we conclude that N_2D^+ only traces parts of the core velocity profile. Following the velocity structure throughout the whole core reveals an overall rotation structure, which is somewhat characteristic of prestellar cores.

The velocity structure is, however, not only characterised by a complex rotation pattern, but the observations of N_2H^+ also reveal a surprising pattern in the linewidth. In large parts of the core, the linewidth can be fully explained with only thermal motions, but a region towards the north-east of SMM1 shows a relatively high non-thermal contribution. This could be induced through outflow activity from the nearby protostar IRS, but also through a possible low-velocity outflow from MMS (CAD12).

5.3. SMM1 – starless or protostellar?

In the previous sections we have established that SMM1 is a slowly rotating dense core in a rather young evolutionary stage (characterised by a flattening of the volume density profile towards the core centre) that is on the verge of being bound. However, the question of whether SMM1 has a starless or a protostellar nature remains.

The key to this question can be the $100 \mu\text{m}$ feature FIRS. Its position and flux density from a preliminary analysis fitted well into the picture of a FHSC at the position of MMS (CAD12). Using our latest calibration and data reduction techniques, we derive a new, more reliable position of FIRS. This new analysis suggests that FIRS is actually offset from MMS by $\sim 7''$. Thanks to the clear detection of IRS in both the $100 \mu\text{m}$ and the 1.3 mm continuum image of CAD12, we can align these two maps to sub-arcsec precision. Additionally, the clear detection of FIRS ($>3\sigma$, Fig. 5) allows us to reach a positional accuracy down to a fraction of the beam size. This suggests that MMS and FIRS are two unrelated features.

This immediately leads to the question of the origin of FIRS. One option is that FIRS is instead associated with both the NIR nebula to the south-east of IRS, and the north-western extension of the large-scale mm-continuum emission SMM2 (see Fig. 1). These three observational features could originate in the working surface associated with the outflow from IRS. In this scenario, the blue-shifted outflow velocities would imply that IRS resides on the far side of the CB 17 cloud. The low-velocity dispersion of N_2H^+ at the position of FIRS would mean that the working surface must be located outside the N_2H^+ emission region at the core edge. Further along its path, the deflected outflow then could penetrate the dense core and stir up material, providing the non-thermal line broadening to the north-east of SMM1.

Thus, the marginal SMA detection of MMS remains the only indication that the dense core SMM is possibly no longer starless in nature, but already contains an embedded FHSC. That MMS can be associated with the position of the N_2H^+ column density peak contradicts the FHSC hypothesis at first glance. The warming up of the central regions should result in the release of CO from the icy grain mantles, which would lead to

the destruction of N_2H^+ . However, if the FHSC has only formed recently, it does not necessarily have to be reflected in an immediately observable change in the N_2H^+ structure. While the new analysis of the Herschel data presented here could not provide additional supporting evidence, it also does not contradict the still unconfirmed FHSC hypothesis. Therefore, the question of whether SMM1 is starless or protostellar remains unanswered until new observational evidence can be presented.

6. Summary

In our study of the isolated Bok globule CB 17, we used FIR and (sub-)mm thermal emission to determine the dust temperature and density structure of CB 17. Interferometric observations of the $\text{N}_2\text{H}^+(1-0)$ transition allowed us to determine the kinematic state of the dense core SMM.

The main conclusions are as follows:

- Using LoS-averaged and ray-tracing fitting routines, we determine the column density and dust temperature distribution of the cometary globule CB 17. We found a peak column density of $N_{\text{H}} = (4.3 \pm 0.3) \times 10^{22} \text{ cm}^{-2}$. The core is approximately spherically symmetric (correcting for ellipticity and excluding IRS from that view) in the central $\sim 18\,000 \text{ au}$, but we observed a progressive decrease in symmetry as the radius increases. We distinguished three regions: The core in the centre, the hot west wing, and the cometary tail.
- For the core region (SMM1), we derived radial temperature and volume density profiles using a RT fitting procedure. We found a mass of $2.3 \pm 0.3 M_{\odot}$. The temperature is found to drop to $\sim 10.6 \pm 0.3 \text{ K}$ in the centre, where we found a central density of $n_{\text{H},0} \sim (2.3 \pm 0.2) \times 10^5 \text{ cm}^{-3}$. The density profile exhibits a flat density plateau out to $r_0 = (9.5 \pm 0.6) \times 10^3 \text{ au}$. An analysis of the temperature and density profiles shows that on a global scale SMM1 is at the margin of being gravitationally bound. This could be the reason it is – although chemically evolved – dynamically still in a very early evolutionary stage.
- The rotation curve of the dense core cannot be explained in simple terms, but we interpreted it as a complex superposition of solid body rotation, together with internal motions of the densest regions.
- We substantiated the finding of FIRS, a small, slightly extended $100 \mu\text{m}$ emission feature at a projected separation of $\sim 3400 \text{ au}$ ($\sim 13.5''$) from IRS. Its position differs slightly from our preliminary result reported in CAD12, which is caused by using the appropriate *Herschel* PSF and a more recent data reduction software. Overall, we found weakened evidence for a FHSC in CB 17. We argued that the sources MMS (CAD12) and FIRS are unrelated, but we cannot determine the true nature of either of these two sources due to the overall complexity of this source and the proximity to IRS.

Looking at the evidence provided by the observations presented in this paper, we can conclude that CB 17 is a source that is in a very early stage of star formation. It remains a key source for studying the conditions of star formation just prior to or in a very early stage of the protostellar collapse. Future observations with upcoming facilities like NOEMA will help shed more light onto the puzzle of CB 17.

Acknowledgements. M.S. acknowledges support from NOVA, the Netherlands Research School for Astronomy. This work was supported by NSF grants 0708158 and 0953142. The work of A.M.S. was supported by the Deutsche Forschungsgemeinschaft priority programme 1573 (“Physics of the

Interstellar Medium”). H.L. was funded by the Deutsches Zentrum für Luft- und Raumfahrt (DLR). This research used the facilities of the Canadian Astronomy Data Centre operated by the National Research Council of Canada with the support of the Canadian Space Agency. The *James Clerk Maxwell* Telescope is operated by the Joint Astronomy Centre on behalf of the Science and Technology Facilities Council of the UK, the Netherlands Organisation for Scientific Research, and the National Research Council of Canada. M.S. acknowledges the use of the GILDAS software package (<http://www.iram.fr/IRAMFR/GILDAS/>).

Appendix A: Energy terms

Gravitational potential energy

The gravitational potential energy is given by

$$E_{\text{grav}} = -4\pi G \int_0^{r_{\text{core}}} M_{\text{r}}(r) n_{\text{H}}(r) \mu_{\text{H}} m_{\text{H}} r \, dr, \quad (\text{A.1})$$

where G is the gravitational constant, $\mu_{\text{H}} = 1.40$ is the mean mass per hydrogen atom (Przybilla et al. 2008), m_{H} is the proton mass, and

$$M_{\text{r}}(r) = 4\pi \mu_{\text{H}} m_{\text{H}} \int_0^r r^2 n_{\text{H}}(r) \, dr, \quad (\text{A.2})$$

is the mass enclosed by a shell with radius r .

The gravitational potential energy is sometimes expressed as $E_{\text{grav}} = -\alpha_{\text{vir}} G M_{\text{core}}^2 / r_{\text{core}}$. Using the volume density profiles derived in the ray-tracing fit, we determine the pre-factor for CB 17 to be $\alpha_{\text{vir}} = 0.82 \pm 0.05$.

Thermal energy

The thermal energy is given by

$$E_{\text{therm}} = \frac{3 k_{\text{B}}}{2} 4\pi \int_0^{r_{\text{core}}} n_{\text{p}}(r) T(r) r^2 \, dr, \quad (\text{A.3})$$

where k_{B} is the Boltzmann constant, and $n_{\text{p}} = n_{\text{H}} \mu_{\text{H}} / \mu_{\text{p}}$ is the volume density of particles with $\mu_{\text{p}} = 2.32$ being the mean atomic mass per particle in molecular clouds (Przybilla et al. 2008).

Rotational energy

The energy for solid-body rotation at an angular frequency ω is

$$E_{\text{rot}} = \frac{1}{2} I \omega^2. \quad (\text{A.4})$$

The moment of inertia I is can be calculated by

$$I = \int_V \mu_{\text{H}} m_{\text{H}} n_{\text{H}}(r) s^2 \, dV \quad (\text{A.5})$$

with s the distance to the rotation axis. Assuming a spherical coordinate system and rotation around the axis with polar angle $\vartheta = 0$ we obtain $s = r \sin \vartheta$. Hence, the moment of inertia is

$$I = 2\pi \mu_{\text{H}} m_{\text{H}} \int_0^{r_{\text{core}}} \int_0^\pi r^4 \sin^3 \vartheta n_{\text{H}}(r) \, d\vartheta \, dr \quad (\text{A.6})$$

$$= \frac{8\pi}{3} \mu_{\text{H}} m_{\text{H}} \int_0^{r_{\text{core}}} r^4 n_{\text{H}}(r) \, dr. \quad (\text{A.7})$$

Turbulent energy

Assuming a Boltzmann-distributed turbulent velocity, the turbulent energy content can be estimated by relating the squared non-thermal line broadening Δv_{NT}^2 to the averaged squared 3D-velocity $\langle v^2 \rangle$. The kinetic energy of the turbulent gas is then given by

$$E_{\text{turb}} = \frac{M_{\text{core}} \langle v^2 \rangle}{2} \quad (\text{A.8})$$

$$= \frac{3 M_{\text{core}} \Delta v_{\text{NT}}^2}{16 \ln(2)}. \quad (\text{A.9})$$

Magnetic energy

Assuming a constant magnetic field strength throughout the core, the magnetic energy is

$$E_{\text{mag}} = \frac{4\pi r_{\text{core}}^3}{3} u_{\text{mag}}, \quad (\text{A.10})$$

where $u_{\text{mag}} = B^2/(2\mu_0)$ is the magnetic energy density, B the magnetic field, and μ_0 the magnetic permeability constant.

References

- André, P., Men'shchikov, A., Bontemps, S., et al. 2010, A&A, 518, L102
 André, P., Di Francesco, J., Ward-Thompson, D., et al. 2013
[\[arXiv:1312.6232\]](#)
 Aniano, G., Draine, B. T., Gordon, K. D., & Sandstrom, K. 2011, PASP, 123, 1218
 Arzoumanian, D., André, Ph., Didelon, P., et al. 2011, A&A, 529, L6
 Belloche, A., Parise, B., van der Tak, F. F. S., et al. 2006, A&A, 454, L51
 Beuther, H., Henning, T., Linz, H., Krause, O., et al. 2010, A&A, 518, L78
 Beuther, H., Linz, H., Tackenberg, J., et al. 2013, A&A, 553, A115
 Bergin, E. A., & Tafalla, M. 2007, ARA&A, 45, 339
 Caselli, P., Myers, P. C., & Thaddeus, P. 1995, ApJ, 455, L77
 Caselli, P., Benson, P. J., Myers, P. C., & Tafalla, M. 2002a, ApJ, 572, 238
 Caselli, P., Walmsley, C. M., Zucconi, A., et al. 2002b, ApJ, 565, 331
 Caselli, P., Keto, E., Bergin, E. A., et al. 2012, ApJ, 759, L37
 Chen, X., Launhardt, R., & Henning, T. 2007, ApJ, 669, 1058
 Chen, X., Arce, H. G., Zhang, Q., et al. 2010, ApJ, 715, 1344
 Chen, X., Arce, H. G., Dunham, M. M., et al. 2012, ApJ, 751, 89
 Clemens, D. P., & Barvainis, R. 1988, ApJS, 68, 257
 Commerçon, B., Launhardt, R., Dullemond, C., & Henning, T. 2012, A&A, 545, A98
 Crapsi, A., Caselli, P., Walmsley, C. M., et al. 2005, ApJ, 619, 379
 Enoch, M. L., Lee, J.-E., Harvey, P., Dunham, M. M., & Schnee, S. 2010, ApJ, 722, L33
 Evans, N. J., II, Rawlings, J. M. C., Shirley, Y. L., & Mundy, L. G. 2001, ApJ, 557, 193
 Evans, N. J., II, Dunham, M. M., Jørgensen, J. K., et al. 2009, ApJS, 181, 321
 di Francesco, J., Evans, N. J., II, Caselli, P., et al. 2007, Protostars and Planets V, 17
 Griffin, M. J., Abergel, A., Abreu, A., et al. 2010, A&A, 518, L3
 Henning, T., Linz, H., Krause, O., et al. 2010, A&A, 518, L95
 Johnstone, D., Rosolowsky, E., Tafalla, M., & Kirk, H. 2010, ApJ, 711, 655
 Jørgensen, J. K., Schöier, F. L., & van Dishoeck, E. F. 2002, A&A, 389, 908
 Kainulainen, J., Ragan, S. E., Henning, T., & Stutz, A. 2013, A&A, 557, A120
 Kane, B. D., & Clemens, D. P. 1997, AJ, 113, 1799
 Lada, C. J., & Lada, E. A. 2003, ARA&A, 41, 57
 Launhardt, R., & Henning, T. 1997, A&A, 326, 329
 Launhardt, R., Nutter, D., Ward-Thompson, D., et al. 2010, ApJS, 188, 139
 Launhardt, R., Stutz, A. M., Schmiedeke, A., et al. 2013, A&A, 551, A98
 Larson, R. B. 1969, MNRAS, 145, 271
 Lemme, C., Wilson, T. L., Tieftrunk, A. R., & Henkel, C. 1996, A&A, 312, 585
 Leung, C. M. 1975, ApJ, 199, 340
 Linz, H., Krause, O., Beuther, H., et al. 2010, A&A, 518, L123
 Lippok, N., Launhardt, R., Semenov, D., et al. 2013, A&A, 560, A41
 Lucy, L. B. 1974, AJ, 79, 745
 Lynds, B. T. 1962, ApJS, 7, 1
 Masunaga, H., Miyama, S. M., & Inutsuka, S.-I. 1998, ApJ, 495, 346
 Matthews, B. C., McPhee, C. A., Fissel, L. M., & Curran, R. L. 2009, ApJS, 182, 143
 Molinari, S., Swinyard, B., Bally, J., et al. 2010, A&A, 518, L100
 Motte, F., Andre, P., & Neri, R. 1998, A&A, 336, 150
 Nielbock, M., Launhardt, R., Steinacker, J., et al. 2012, A&A, 547, A11
 Ossenkopf, V., & Henning, T. 1994, A&A, 291, 943
 Omukai, K. 2007, PASJ, 59, 589
 Pavlyuchenkov, Y., Wiebe, D., Launhardt, R., & Henning, T. 2006, ApJ, 645, 1212
 Pavlyuchenkov, Y., Henning, T., & Wiebe, D. 2007, ApJ, 669, L101
 Pezzuto, S., Elia, D., Schisano, E., et al. 2012, A&A, 547, A54
 Pilbratt, G. L., Riedinger, J. R., Passvogel, T., et al. 2010, A&A, 518, L1
 Pineda, J. E., Arce, H. G., Schnee, S., et al. 2011, ApJ, 743, 201
 Pittan, J., Linz, H., Ragan, S., et al. 2013, ApJ, 766, 68
 Poglitsch, A., Waelkens, C., Geis, N., et al. 2010, A&A, 518, L2
 Przybilla, N., Nieva, M.-F., & Butler, K. 2008, ApJ, 688, L103
 Ragan, S., Henning, Th., Krause, O., et al. 2012, A&A, 547, A49
 Richardson, W. H. 1972, J. Opt. Soc. Am. (1917–1983), 62, 55
 Roussel, H. 2013, PASP, 125, 1126
 Saigo, K., Tomisaka, K., & Matsumoto, T. 2008, ApJ, 674, 997
 Shirley, Y. L., Evans, N. J., II, Rawlings, J. M. C., & GregerSEN, E. M. 2000, ApJS, 131, 249
 Shu, F. H. 1977, ApJ, 214, 488
 Sodroski, T. J., Odegard, N., Arendt, R. G., et al. 1997, ApJ, 480, 173
 Stutz, A., Launhardt, R., Linz, H., et al. 2010, A&A, 518, L87
 Stutz, A. M., Tobin, J. J., Stanke, T., et al. 2013, ApJ, 767, 36
 van der Tak, F. F. S., Black, J. H., Schöier, F. L., Jansen, D. J., & van Dishoeck, E. F. 2007, A&A, 468, 627
 Tafalla, M., Myers, P. C., Caselli, P., & Walmsley, C. M. 2004, A&A, 416, 191
 Taquet, V., Peters, P. S., Kahane, C., et al. 2013, A&A, 550, A127
 Tomida, K., Tomisaka, K., Matsumoto, T., Ohsuga, et al. 2010, ApJ, 714, L58
 Walsh, A. J., Myers, P. C., & Burton, M. G. 2004, ApJ, 614, 194
 Ward-Thompson, D., Scott, P. F., Hills, R. E., & Andre, P. 1994, MNRAS, 268, 276
 Ward-Thompson, D., Motte, F., & Andre, P. 1999, MNRAS, 305, 143
 Ward-Thompson, D., André, P., & Kirk, J. M. 2002, MNRAS, 329, 257
 Womack, M., Ziurys, L. M., & Wyckoff, S. 1992, ApJ, 387, 417
 Young, C. H., Jørgensen, J. K., Shirley, Y. L., et al. 2004, ApJS, 154, 396
 Zucconi, A., Walmsley, C. M., & Galli, D. 2001, A&A, 376, 650